Efficient Calculation Method and Characterization of Flux Density Distribution in Nanocrystalline Core of High-Frequency Transformer Under Load Condition

Zhanlei Liu, *Graduate Student Member, IEEE*, Lingyu Zhu, *Senior Member, IEEE*, Yongliang Dang, and Shengchang Ji, *Member, IEEE*

***Abstract*—Core loss is determined by flux density distribution. Since main flux density is uniform and leakage flux density is concentrated in surface ribbons of nanocrystalline core in high-frequency transformer (HFT), practical flux density in nanocrystalline core under load condition may be nonuniform. This article proposes an efficient flux density distribution calculation method for nanocrystalline core of HFT under load condition, namely operating condition decomposition-based method (OCDEM). The load condition is decomposed into open-circuit and short-circuit conditions. The practical flux density is proposed to be calculated by summation of main flux density under open-circuit excitation and leakage flux density under short-circuit excitation. Compared with time-domain FE and frequency-domain decomposition FE methods, the proposed OCDEM reduces computation time and achieves high calculation accuracy. Furthermore, flux density distribution characteristics in nanocrystalline core are studied. Calculation results show that flux density amplitude in surface ribbons is higher than interior ribbons and that in winding end is higher than other positions. Flux density amplitude in surface ribbons increases with permeability and that in interior ribbons decrease with permeability. Finally, infrared and calorimetric measurement results show the nonuniform flux density distribution increases core temperature and loss. The obtained characteristics can guide the HFT design.**

***Index Terms*—Flux density distribution, high-frequency transformer, load condition, nanocrystalline core, operating condition decomposition.**

I. Introduction

HIGH-FREQUENCY transformer (HFT) is a vital component in power electronic transformers [1], [2], [3], [4], [5], [6], providing galvanic isolation and power transmission among ac–dc ports [7], [8], [9]. Taking advantages of high saturated flux density and low loss density, nanocrystalline core is usually preferred in high-voltage and high-power HFT [10].

Accurate estimation of core loss is significant for accurate temperature prediction and reliable thermal design of HFT [9], [11], [12], [13]. Since core loss density is dependent on magnetic flux density waveform and amplitude, the overall core loss of HFT will depend on magnetic flux density distribution in the core. In [14] and [15], a film resistor is connected to the secondary winding of HFT to conduct load experiment. It is revealed that flux densities in the core decrease with load current due to the increase of voltage drops across the windings. However, the core material studied in these articles are ferrite instead of nanocrystalline. In addition, flux density distribution characteristics under DAB load condition have not been investigated.

Ferrite core shows isotropic permeability and conductivity. Therefore, leakage flux can penetrate into interior core and be uniformly distributed in the core section. However, nanocrystalline core, which is made by rolling of nanocrystalline ribbons, shows anisotropic permeability and conductivity due to its laminated structure [16], [17], [18]. In open-circuit conditions, when nanocrystalline core is nongapped, due to the difference in magnetic reluctance, flux density in the inner layers of nanocrystalline ribbons is slightly higher than the outer layers. When nanocrystalline core is gapped, due to fringing flux around the air gap, the equivalent reluctance of surface ribbons is lower than interior ribbons. Thus, flux density in the inner and outer surface ribbons may be higher than interior ribbons [19]. In short-circuit conditions, since permeability of epoxy resin is low, the equivalent permeability of nanocrystalline core in laminated direction is much lower than rolling direction and thickness direction. Therefore, leakage flux density is mainly concentrated in the surface ribbons [20], [21], [22], [23]. However, characteristics of flux density distribution in nanocrystalline core of HFT under load condition have not been well understood yet.

The practical flux in nanocrystalline core of HFT under load condition is the summation of main flux and leakage flux, as shown in Fig. 1. Since main flux is relatively uniform over the core cross-section and leakage flux is mainly concentrated in the surface of the core, practical flux density distribution in nanocrystalline core can be nonuniform. The nonuniform flux density distribution characteristics will be investigated in this article. In addition, the words “inner layer,” “outer layer,” and “interior” are explained in Fig. 1, which are used in this article.

Finite element (FE) simulation provides an approach for calculating flux density distribution in magnetic core. Since nanocrystalline ribbon is very thin, fine-meshing of each layer of ribbon in the nanocrystalline core can generate a large number

Received 6 May 2025; revised 2 August 2025; accepted 12 September 2025. Date of publication 16 September 2025; date of current version 23 December 2025. Recommended for publication by Associate Editor D. Oliveira. *(Corresponding author: Lingyu Zhu.)*

The authors are with the State key Laboratory of Electrical Insulation and Power Equipment, Xi’an Jiaotong University, Xi’an 710049, China (e-mail: lzl0283@stu.xjtu.edu.cn; zhuly1026@xjtu.edu.cn; dyl877759724@stu.xjtu.edu.cn; jsc@xjtu.edu.cn).

Color versions of one or more figures in this article are available at https://doi.org/10.1109/TPEL.2025.3610516.

Digital Object Identifier 10.1109/TPEL.2025.3610516

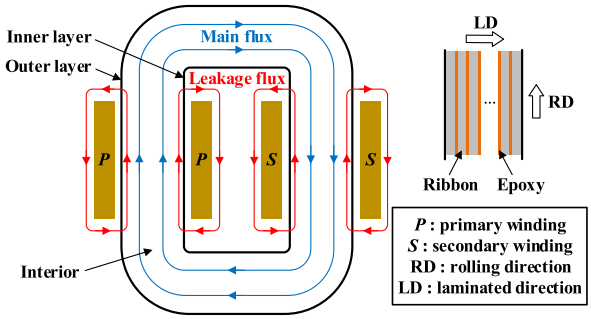

Fig. 1. Schematic diagram of flux distribution in nanocrystalline core of HFT under load condition.

of meshes. To reduce the mesh numbers in FE model, homogenization approaches are adopted in [16], [17], [18], [19], [20], [21], and [23]. To accurately calculate the leakage flux density in surface ribbons, fine-meshing of surface ribbons is still required, which increases the mesh numbers and computation time. In addition, J. Wang et al. [16], Y. Wang et al. [17], Calderon-Lopez et al. [18], Sun et al. [19], Beddingfield et al. [20], Chen et al. [21], and Liu et al. [23] only calculate the flux density under sinusoidal excitation by frequency-domain simulation. Calculation of flux density distribution under nonsinusoidal excitation of load condition by time-domain simulation will further increase the computation time. An accurate and efficient calculation method of flux density distribution in nanocrystalline core of HFT under load condition is demanding.

To address the aforementioned problems, this article proposes an accurate and efficient calculation method of flux density distribution in nanocrystalline core under load condition and investigates the flux density distribution characteristics. The main contributions of this article are summarized as follows.

1) An efficient flux density distribution calculation method for nanocrystalline core of HFT under load condition is proposed, namely operating condition decomposition-based method (OCDEM). The practical load condition is decomposed into open-circuit condition and short-circuit condition. Based on flux superposition principle, the practical flux density in nanocrystalline core is proposed to be calculated by summation of main flux density under open-circuit excitation and leakage flux density under short-circuit excitation. Compared with time-domain FE and frequency-domain decomposition FE methods, the proposed OCDEM improves the computation efficiency and achieves high calculation accuracy.
2) The flux variation rate $\mathrm{d}\phi(t)/\mathrm{d}t$ through surface ribbons of nanocrystalline core is discovered to be four-level stair wave instead of square wave for load condition of DAB converter with single-phase-shift (SPS) modulation. Flux density concentration in surface ribbons of nanocrystalline core is discovered and the nonuniform flux density distribution characteristics are investigated.
3) The impact of nonuniform flux density distribution or surface flux density concentration on nanocrystalline core loss is discussed. Infrared measurement results show that the nonuniform flux density distribution increases core temperature. Calorimetric measurement results show that the nonuniform flux density distribution increases core loss by 10%–30% and 40%–60% for nanocrystalline core HFT with concentric windings and separated windings, respectively.

It should be noted that the surface ribbons of nanocrystalline core may saturate under load condition due to the concentration of leakage flux density. The surface ribbons saturation will change the practical flux density distribution and core loss. However, flux density distribution calculation considering surface ribbons saturation is very difficult due to the nonlinear *B-H* relationship. In this article, the proposed OCDEM aims to calculate the flux density distribution under unsaturated condition. The saturation effect and nonlinear *B-H* relationship are not considered, and thus, flux superposition principle can be applied. In our another paper [24], the impact of surface ribbons saturation on core loss is analyzed in detail and accurate calculation methods of leakage flux induced power loss considering surface ribbons saturation are proposed. The proposed calculation methods are based on accurate flux density distribution calculation. Our previous paper [24] mainly focuses on leakage flux induced power loss calculation methods and only briefly explains the flux density calculation procedure. This article gives detailed formula derivations, effective experimental validations, and thorough flux density distribution characteristic analysis, thus enabling a better understanding of the practical flux density distribution to guide the power loss calculation and optimal design of HFT.

The rest of this article is organized as follows. In Section II, the principle and calculation procedure of the proposed OCDEM are introduced. A DAB converter with SPS modulation is taken as a case of load condition to illustrate the proposed method in detail. In Section III, a DAB converter with SPS modulation is built. The waveforms of flux variation rate $\mathrm{d}\phi(t)/\mathrm{d}t$ are analyzed. The accuracy of proposed OCDEM is verified by experiments. The accuracy and efficiency of proposed OCDEM are compared with time-domain FE and frequency-domain decomposition FE methods. In Section IV, the practical flux density distribution characteristics are investigated. In Section V, the impact of nonuniform flux density distribution on core loss is discussed. Finally, Section VI concludes this article.

II. Calculation Method of Practical Flux Density Distribution

Since magnetic flux density cannot be measured directly, an equivalent magnetization voltage (EMV) $u_{\mathrm{m}}(S, t)$ is proposed in this article, leveraging Faraday's electromagnetic induction law, to characterize the average flux density through a core section S. The $u_{\mathrm{m}}(S, t)$ can be expressed as

$$u_{\mathrm{m}}(S,t)=\frac{\mathrm{d}\phi(S,t)}{\mathrm{d}t}=\frac{\mathrm{d}}{\mathrm{d}t}\int B(t)\mathrm{d}S=S\frac{\mathrm{d}B_{\mathrm{ave}}(S,t)}{\mathrm{d}t} \quad (1)$$

where $u_{\mathrm{m}}(S,t)$ is EMV of core section S, $\phi(S,t)$ is magnetic flux through core section S, B(t) is flux density, and $B_{\mathrm{ave}}(S,t)$ is average flux density of core section S. The EMV $u_{\mathrm{m}}(S,t)$ of a core section S can be measured on a single-turn open-circuited coil tightly wound around this core section. The schematic diagram of time-domain waveforms $u_{\mathrm{m}}(S,t)$ and $B(t)$ is shown in Fig. 2.

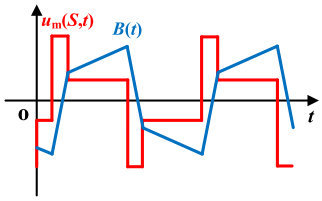

Fig. 2. Schematic diagram of time-domain waveforms $u_m(S,t)$ and $B(t)$.

Time-domain FE simulation of practical flux density distribution in nanocrystalline core by homogenization FE model [16], [17], [18] is very time-consuming. In this section, an accurate and efficient flux density distribution calculation method for nanocrystalline core of HFT under load condition, namely OCDEM, is proposed.

A. Principle of Proposed Method

When magnetic core is not saturated, permeability μ is constant. According to the superposition principle of linear system, the practical load condition can be decomposed into open-circuit condition and short-circuit condition. Therefore, the practical flux through a core section S under load condition $\phi_{\text{load}}(S,t)$ can be calculated by summation of main flux $\phi_{\text{main}}(S,t)$ and leakage flux $\phi_{\text{leakage}}(S,t)$

$$\phi_{\text{load}}(S,t) = \phi_{\text{main}}(S,t) + \phi_{\text{leakage}}(S,t). \tag{2}$$

The main flux $\phi_{\text{main}}(S,t)$ comes from open-circuit voltage excitation and leakage flux $\phi_{\text{leakage}}(S,t)$ comes from short-circuit voltage excitation. Using (1), the practical EMV of a core section S under load condition $u_{\text{m,load}}(S,t)$ can be calculated by summation of main flux induced EMV under open-circuit condition $u_{\text{m,open}}(S,t)$ and leakage flux induced EMV under short-circuit condition $u_{\text{m,short}}(S,t)$

$$u_{\text{m,load}}(S,t) = u_{\text{m,open}}(S,t) + u_{\text{m,short}}(S,t). \tag{3}$$

Taking DAB converter with SPS modulation as an example, the decomposition and superposition procedure is illustrated in Fig. 3. The primary voltage $u_{\text{AB}}(t)$ and secondary voltage $u_{\text{CD}}(t)$ of HFT are square wave. According to electric circuit superposition principle, the practical voltage excitation of HFT with $u_{\text{AB}}(t)$ and $u_{\text{CD}}(t)$ can be decomposed into open-circuit excitation with $u_{\text{CD}}(t)$ and $u_{\text{CD}}(t)$ and short-circuit excitation with $u_{\text{AB}}(t)$-$u_{\text{CD}}(t)$ and 0. The main flux comes from the open-circuit excitation where both primary and secondary voltages are $u_{\text{CD}}(t)$, and leakage flux comes from the short-circuit excitation where primary voltage is $u_{\text{AB}}(t)$-$u_{\text{CD}}(t)$ and secondary voltage is zero. The practical flux under load condition is summation of main flux and leakage flux. According to (3), the EMV under load condition is the summation of main flux induced EMV under open-circuit condition and leakage flux induced EMV under short-circuit condition.

The EMVs under open-circuit and short-circuit excitations can be calculated as

$$u_{\text{m,open}}(S,t) = k_1(S)u_{\text{open}}(t) \tag{4}$$

$$u_{\text{m,short}}(S,t) = k_2(S)u_{\text{short}}(t) \tag{5}$$

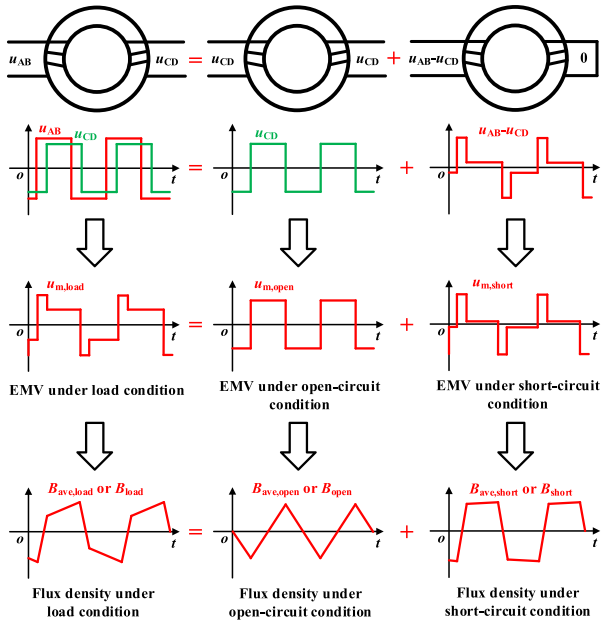

Fig. 3. Schematic diagram of practical EMV and flux density calculation under load condition of DAB converter with SPS modulation.

where $u_{\text{open}}(t)$ and $u_{\text{short}}(t)$ are open-circuit excitation voltage and short-circuit excitation voltage, $k_1(S)$ and $k_2(S)$ are coefficients related to the main flux and leakage flux distributions in the core section S under open-circuit and short-circuit sinusoidal excitations.

Combining (3)–(5), the practical EMV of a core section S under load condition can be expressed as

$$u_{\text{m,load}}(S,t) = k_1(S)u_{\text{open}}(t) + k_2(S)u_{\text{short}}(t). \tag{6}$$

For the load condition of DAB converter as shown in Fig. 3, the practical EMV of the core section S can be expressed as

$$u_{\text{m,DAB}}(S,t) = k_{1,\text{DAB}}(S)u_{\text{CD}}(t) + k_{2,\text{DAB}}(S)(u_{\text{AB}}(t) - u_{\text{CD}}(t)) \tag{7}$$

By integral operation or inverse operation of (1), average flux density through the core section S can be expressed as

$$\begin{aligned} B_{\text{ave}}(S,t) &= \frac{1}{S}\int u_{\text{m,load}}(S,t)\text{d}t \\ &= \frac{1}{S}\int (k_1(S)u_{\text{open}}(t) + k_2(S)u_{\text{short}}(t))\text{d}t. \end{aligned} \tag{8}$$

When the section area S approaches zero, (8) becomes

$$\begin{aligned} B(x,y,z,t) &= \lim_{S\to 0}\frac{1}{S}\int (k_1(S)u_{\text{open}}(t) + k_2(S)u_{\text{short}}(t))\text{d}t \\ &= \lim_{S\to 0}\frac{1}{S}\int (k_1(S)u_{\text{open}}(t)\text{d}t + k_2(S)u_{\text{short}}(t)\text{d}t) \\ &= \lim_{S\to 0}\frac{1}{S}(k_1(S)\psi_{\text{main}}(t) + k_2(S)\psi_{\text{leak}}(t)) \\ &= k_{11}(x,y,z)\psi_{\text{main}}(t) + k_{22}(x,y,z)\psi_{\text{leak}}(t) \end{aligned} \tag{9}$$

where $B(x,y,z,t)$ is flux density waveform at coordinate (x,y,z), $\psi_{\text{main}}(t)$, and $\psi_{\text{leak}}(t)$ are main flux linkage under open-circuit voltage condition and leakage flux linkage under short-circuit

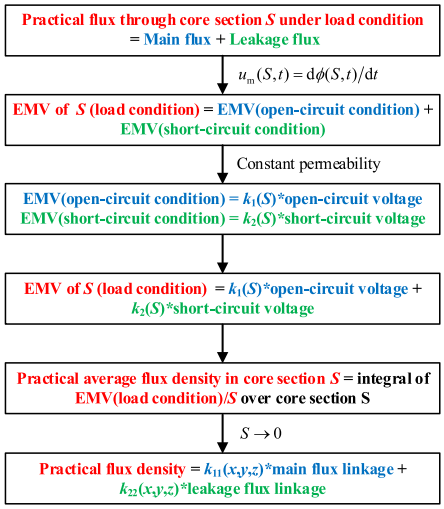

Fig. 4. Schematic diagram of proposed calculation method of practical flux density distribution.

voltage condition, $k_{11}(x,y,z)$ and $k_{22}(x,y,z)$ are coefficients related to main flux density and leakage flux density distributions under open-circuit and short-circuit sinusoidal voltage excitations

$$\psi_{\text{main}}(t) = \int u_{\text{open}}(t) \cdot \mathrm{d}t \tag{10}$$

$$\psi_{\text{leak}}(t) = \int u_{\text{short}}(t) \cdot \mathrm{d}t \tag{11}$$

$$k_{11}(x,y,z) = \lim_{S\to 0} \frac{k_1(S)}{S} \tag{12}$$

$$k_{22}(x,y,z) = \lim_{S\to 0} \frac{k_2(S)}{S}. \tag{13}$$

The simplified schematic diagram of the proposed method is illustrated in Fig. 4.

The coefficients $k_1(S)$, $k_2(S)$, $k_{11}(x,y,z)$, and $k_{22}(x,y,z)$ under open-circuit and short-circuit nonsinusoidal excitations can be assumed equal to that under open-circuit and short-circuit sinusoidal excitations with the same frequencies. The coefficients $k_1(S)$, $k_2(S)$, $k_{11}(x,y,z)$, and $k_{22}(x,y,z)$ under open-circuit or short-circuit sinusoidal excitations can be calculated by FE simulations. First, flux density distributions in nanocrystalline core of HFT under open-circuit and short-circuit excitations are calculated by frequency-domain FE simulations. In open-circuit FE simulation, the secondary winding of HFT is open-circuited and the primary winding is excited with sinusoidal voltage of 1 V peak value. In short-circuit FE simulation, the secondary winding of HFT is short-circuited and the primary winding is excited with sinusoidal voltage of 1 V peak value. Then, the EMV amplitude $U_{\text{m}}(S)$ of a core section S can be calculated by

$$\begin{aligned} U_{\text{m}}(S) &= \omega\phi_{\text{m}}(S) = \omega \int B_{\text{m}}(x,y,z) \cdot \mathrm{d}S \\ &= 2\pi f \int B_{\text{m}}(x,y,z) \cdot \mathrm{d}S \end{aligned} \tag{14}$$

where f is frequency, $\phi_{\text{m}}(S)$ is amplitude of flux through the core section S, $\text{B}_{\text{m}}(x,y,z)$ is flux density amplitude at coordinate (x,y,z).

Finally, $k_1(S)$, $k_2(S)$, $k_{11}(x,y,z)$, and $k_{22}(x,y,z)$ can be calculated by

$$k_1(S) = U_{\text{m,open}}(S)/U_{\text{sin,open}} \tag{15}$$

TABLE I
PARAMETERS IN THE HOMOGENIZATION FE MODEL

F	μ_{m}	σ_{m}(S/m)	μ_{r} and μ_{d}	μ_{n}	σ_{r} and σ_{d}(S/m)	σ_{n}(S/m)
0.8	35 000	8.7×10^5	28 000	5	6.78×10^5	0.4955

$$k_2(S) = U_{\text{m,short}}(S)/U_{\text{sin,short}} \tag{16}$$

$$k_{11}(x,y,z) = \lim_{S\to 0} \frac{U_{\text{m,open}}(S)/S}{U_{\text{sin,open}}} = \frac{B_{\text{m,open}}(x,y,z)}{\psi_{\text{main,m}}} \tag{17}$$

$$k_{22}(x,y,z) = \lim_{S\to 0} \frac{U_{\text{m,short}}(S)/S}{U_{\text{sin,short}}} = \frac{B_{\text{m,short}}(x,y,z)}{\psi_{\text{leak,m}}} \tag{18}$$

where $U_{\text{m,open}}(S)$ and $U_{\text{m,short}}(S)$ are EMV amplitudes under open-circuit and short-circuit conditions of the core section S calculated by FE models, $B_{\text{m,open}}(x,y,z)$ and $B_{\text{m,short}}(x,y,z)$ are flux density amplitude distributions under open-circuit and short-circuit conditions calculated by FE models, $U_{\text{sin,open}}$ and $U_{\text{sin,short}}$ are open-circuit and short-circuit excitation voltage amplitudes, $\psi_{\text{main,m}}$ and $\psi_{\text{leak,m}}$ are main flux linkage and leakage flux linkage amplitudes under open-circuit and short-circuit excitations. According to (10) and (11), by phasor method

$$\psi_{\text{main,m}} = U_{\text{sin,open}}/2\pi f \tag{19}$$

$$\psi_{\text{leak,m}} = U_{\text{sin,short}}/2\pi f. \tag{20}$$

Since the conductivity and permeability of nanocrystalline core are anisotropy, homogenization FE model [16], [17], [18] is adopted to calculate the flux density distributions. The nanocrystalline core is modeled with a solid continuum of anisotropic conductivity and permeability instead of a fine laminated structure. The nanocrystalline alloy used in this article is Fe-based nanocrystalline alloy from Advanced Technology and Materials Co., Ltd., in China. The specific composition is $\text{Fe}_{73.5}\text{Cu}_1\text{Nb}_3\text{Si}_{15.5}\text{B}_7$. The thickness of the ribbon is about 18 μm and the filling factor F is about 0.8. The parameters of the homogenized nanocrystalline core model at 20 kHz are listed in Table I, where μ_{r}, μ_{d}, and μ_{n} are equivalent permeability in rolling direction, thick direction and normal direction of the core, σ_{r}, σ_{d}, and σ_{n} are equivalent conductivity in rolling direction, thick direction, and normal direction of the core, μ_{m} is permeability of the ribbon, σ_{m} is conductivity of the ribbon.

B. Calculation Procedure With Proposed Method

The flux density distribution calculation procedure with the proposed OCDEM is shown in Fig. 5 and described as follows.

Step 1: Decompose the load condition into open-circuit condition and short-circuit condition with the decomposition method introduced in Section II-A and shown in Fig. 3.

Step 2: Calculate main flux linkage amplitude under open-circuit voltage excitation by (19) and leakage flux linkage amplitude under short-circuit voltage excitation by (20).

Step 3: Establish a FE model for HFT, in which the nanocrystalline core is modeled by homogenization FE approach.

Step 4: Implement frequency-domain FE simulations under open-circuit and short-circuit excitations to calculate the flux

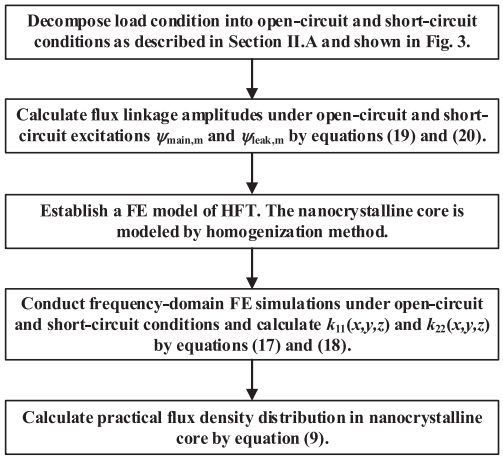

Fig. 5. Flux density distribution calculation procedure with proposed OCDEM.

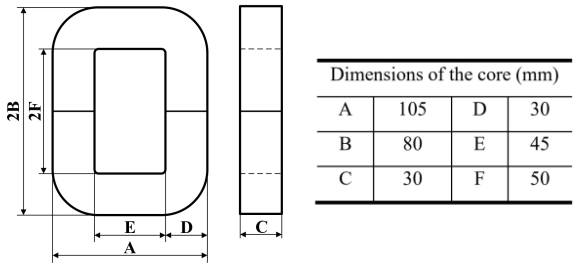

Dimensions of the core (mm)			
A	105	D	30
B	80	E	45
C	30	F	50

Fig. 6. Dimensions of the UU-shape core selected in this article.

density distributions in nanocrystalline core. Calculate the coefficients $k_{11}(x,y,z)$ and $k_{22}(x,y,z)$ by (17) and (18) with the calculated flux density distributions.

Step 5: Calculate the practical flux density distribution in nanocrystalline core by (9).

C. Discussion

The DAB converter with SPS modulation is merely taken as a case of load condition to explain the proposed method. Flux density distribution in nanocrystalline core of HFT operated in other topology circuits or under other load conditions can also be calculated with the proposed method.

As shown in (9)–(11) and Fig. 5, the flux density distribution is calculated with $k_{11}(x,y,z)$, $k_{22}(x,y,z)$, $u_{\rm open}(t)$, and $u_{\rm short}(t)$. The $k_{11}(x,y,z)$ and $k_{22}(x,y,z)$ are determined by HFT structure and calculated by FE method. The $u_{\rm open}(t)$ and $u_{\rm short}(t)$ are derived from primary and secondary voltage waveforms of HFT, which are determined by the circuit topology and modulation strategy. Therefore, to calculate the flux density distribution in nanocrystalline core HFT under other topologies such as *LLC* or PSFB, the first step is determination of primary and secondary voltage waveforms of HFT $u_{\rm AB}(t)$ and $u_{\rm CD}(t)$ based on the circuit topology. The second step is calculation of $k_{11}(x,y,z)$ and $k_{22}(x,y,z)$ with the proposed FE method. After deriving $u_{\rm AB}(t)$ and $u_{\rm CD}(t)$ and calculating $k_{11}(x,y,z)$ and $k_{22}(x,y,z)$, the flux density distribution can be calculated by (9)–(11).

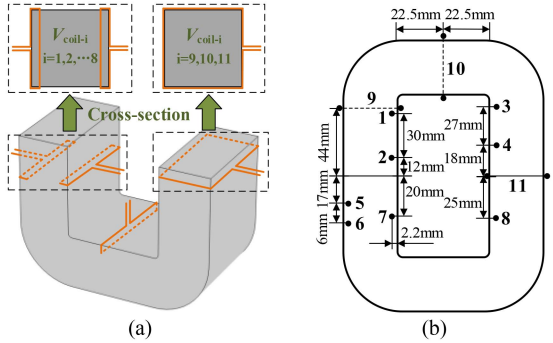

Fig. 7. Customized nanocrystalline core. (a) Overall schematic diagram. (b) Dimensions of embedded wires.

Fig. 8. (a) HFT prototype with separated winding. (b) Customized nanocrystalline core with embedded measurement coils.

III. Experimental Verification

Since flux density cannot be measured directly, EMVs of core sections will be measured to verify the accuracy of the proposed method. In this section, a nanocrystalline core with embedded enameled wires is customized. The EMVs of core cross sections can be measured on the single-turn open-circuited coils tightly wound around these cross sections. A SPS DAB experimental platform is established to verify the accuracy of proposed flux density calculation method.

A. Experimental Setup

A UU-shape nanocrystalline core is selected in this article. The dimensions of the UU core is shown in Fig. 6. To measure the EMV and investigate the practical flux density distribution, several fine enameled wires are embedded inside the core in production phase. Fig. 7(a) shows the overall schematic diagram of the customized nanocrystalline core. Coils 1–8 only surround a thin surface layer of nanocrystalline ribbons and thus measures the EMV of surface ribbons. Coils 9–11 surround the whole cross-section of nanocrystalline core and thus measures the EMV of the whole core cross-section. Fig. 7(b) shows the detailed dimensions of the embedded wires. These 11 coils are located at different positions of the core. The thickness of the measured surface ribbon layer is 2.2 mm.

The HFT prototype tested in this article is shown in Fig. 8. The windings are made by Litz wires. The primary and secondary windings are parallel and wound on the left core leg with coils

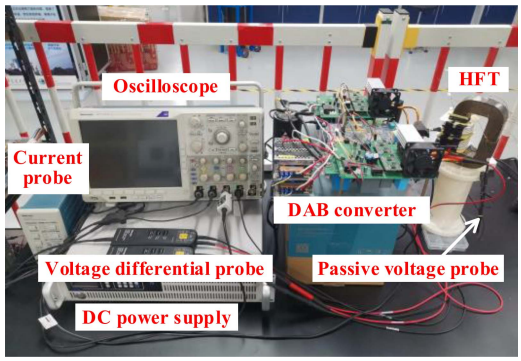

Fig. 9. DAB experimental platform for measurement of practical flux distribution in HFT.

1/2 and 5–7. The turn ratio of primary and secondary winding is 10:10. The leakage inductance is 19.4 μH measured by an impedance analyzer.

A SPS DAB experimental platform is established as shown in Fig. 9. The DAB converter is composed of a dc power supply, two H-bridge modules, a DSP controller, and a HFT. The dc power supply can output maximum voltage and current of 1000 V and 2 A. The MOSFETs used in the H-bridge modules are IPW60R018CFD7 from Infineon. The switching frequency is 20 kHz. The DSP controller is TMS320F28335. Two differential voltage probes are used to measure the primary and secondary voltages of HFT. A current probe is used to measure the current of HFT. A passive voltage probe is used to measure the voltage of measurement coils.

B. Experimental Results

The waveforms of primary and secondary voltages, secondary current and EMVs of the HFT with separated windings are shown in Fig. 10. The primary and secondary voltages are square wave and the amplitude of the square wave voltage is 100 V. The phase shift angle between primary and secondary voltage is 25°. This test condition is referred to as condition I in this article. The peak current of secondary winding is about 20 A. The waveforms of coils voltage or EMV are four-level stair wave instead of square wave. In the nonphase-offset stage (stage 1) when the instantaneous values of primary and secondary voltages are identical, the voltages of coils 1–8 are similar and the voltages of coils 9–11 are similar. In addition, according to Faraday's electromagnetic induction law, $u(t) = N\mathrm{d}\phi(t)/\mathrm{d}t$, the $\mathrm{d}\phi(t)/\mathrm{d}t$ in this stage is close to that under open-circuit condition with the same square voltage excitation. In the phase-offset stage (stage 2) when the instantaneous values of primary and secondary voltages are opposite, the absolute values of voltages of coils 1–9 are higher than that in stage 1, while the absolute values of voltages of coils 10 and 11 are lower than that in stage 1. It is revealed that flux or average flux density varies at different positions of the core and the practical flux density distribution is nonuniform. This flux density distribution difference can be attributed to concentration of leakage flux on the surface ribbons of nanocrystalline core.

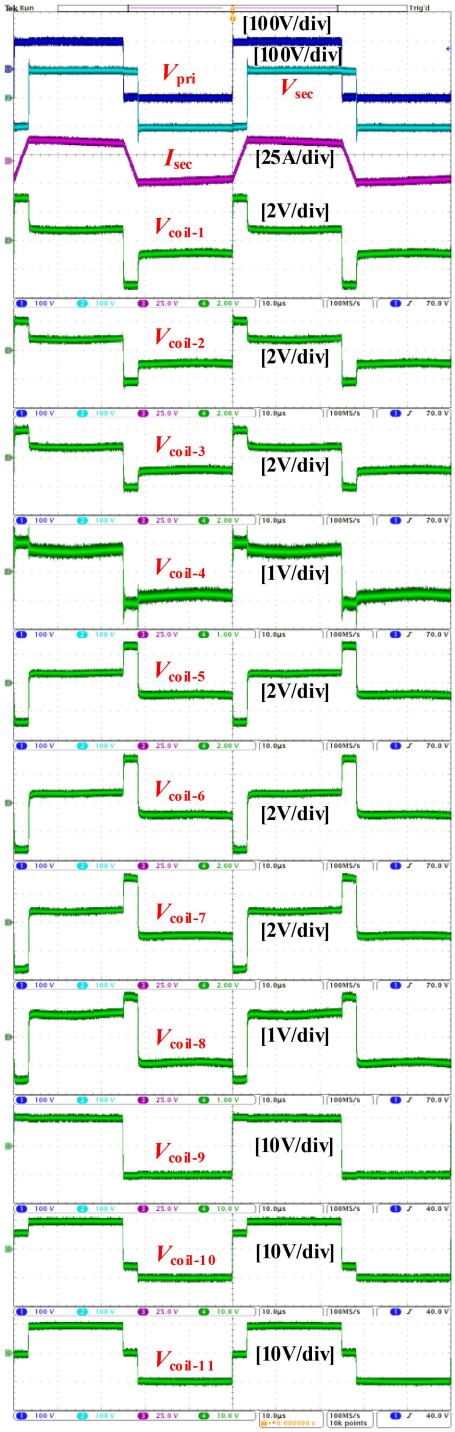

Fig. 10. Waveforms of primary voltage V_{pri}, secondary voltage V_{sec}, secondary current I_{sec}, and equivalent magnetization voltage or coil voltage $V_{\mathrm{coil}\text{-}i}$ of the HFT with separated windings for Condition I ($V_{\mathrm{pri}} = V_{\mathrm{sec}} = 100$ V, phase shift angle $\varphi = 25°$).

C. Validation of Proposed Calculation Method

A small air gap exists in the split point of two U-shape cores. Length of air gap can affect the main flux and leakage flux distribution. To estimate the air gap length, magnetizing inductance of the HFT is measured by an impedance analyzer.

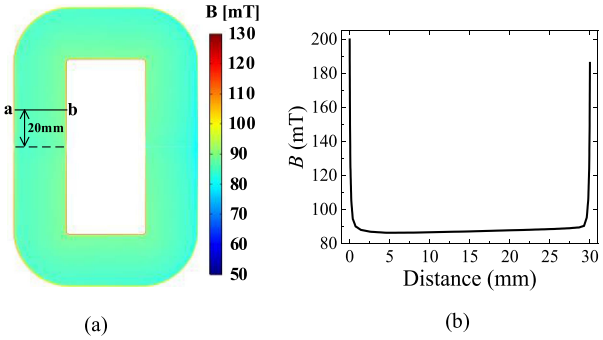

Fig. 11. (a) Main flux density distribution and (b) main flux density along line a-b in nanocrystalline core for the HFT with separated windings under open-circuit sinusoidal excitation with voltage amplitude of 100 V.

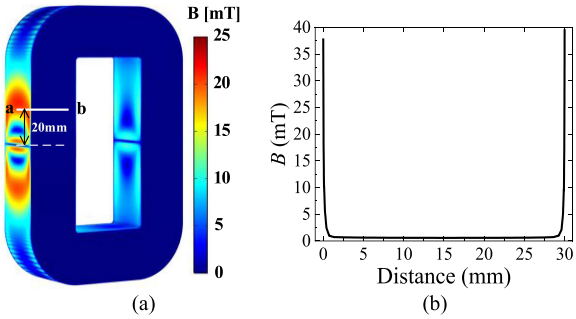

Fig. 12. (a) Leakage flux density distribution and (b) leakage flux density along line a-b in nanocrystalline core for the HFT with separated windings under short-circuit sinusoidal excitation with voltage amplitude of 1 V.

With (21) and (22), the length of air gap is about 0.07 mm

$$\mu = \mu_0 \mu_\mathrm{r} = L_\mathrm{m} \frac{l}{N^2 d_1 d_2} \tag{21}$$

$$\frac{l_\mathrm{nano}}{\mu_\mathrm{nano} F d_1 d_2} + \frac{l_\mathrm{air}}{\mu_0 (d_1 + l_\mathrm{air})(d_2 + l_\mathrm{air})} = \frac{l}{\mu_\mathrm{r} d_1 d_2} \tag{22}$$

where N is number of turns, l is magnetic circuit length of nanocrystalline core, d_1 and d_2 are length and width of core section, l_nano and l_air are the magnetic circuit length of nanocrystalline ribbons and air gap, μ_nano is permeability of nanocrystalline ribbon.

Figs. 11 and 12 show the main flux density and leakage flux density distribution in nanocrystalline core with 0.07 mm air gap. Due to the fringing flux around the air gap, main flux density in the surface ribbons is higher than interior ribbons. Since equivalent permeability in laminated direction of the core is low, leakage flux is mainly concentrated in surface ribbons. The main flux density in the surface ribbon is about 2.3 times of interior ribbons, while the leakage flux density in surface ribbons is about 66 times of interior ribbons. Since the proportion of leakage flux density in surface ribbons to interior ribbons is much higher than main flux density, k_2 is much higher than k_1 in (6) for the surface ribbons, which results in the four-level stair waveforms for EMV of surface ribbons, as shown in Fig. 8 and nonuniform flux density distribution in the core.

The comparisons of calculated and measured EMVs for condition I ($V_\mathrm{pri} = V_\mathrm{sec} = 100$ V, phase shift angle $\varphi = 25°$) are shown in Fig. 13. The calculation results of EMV waveforms coincide with measurement results.

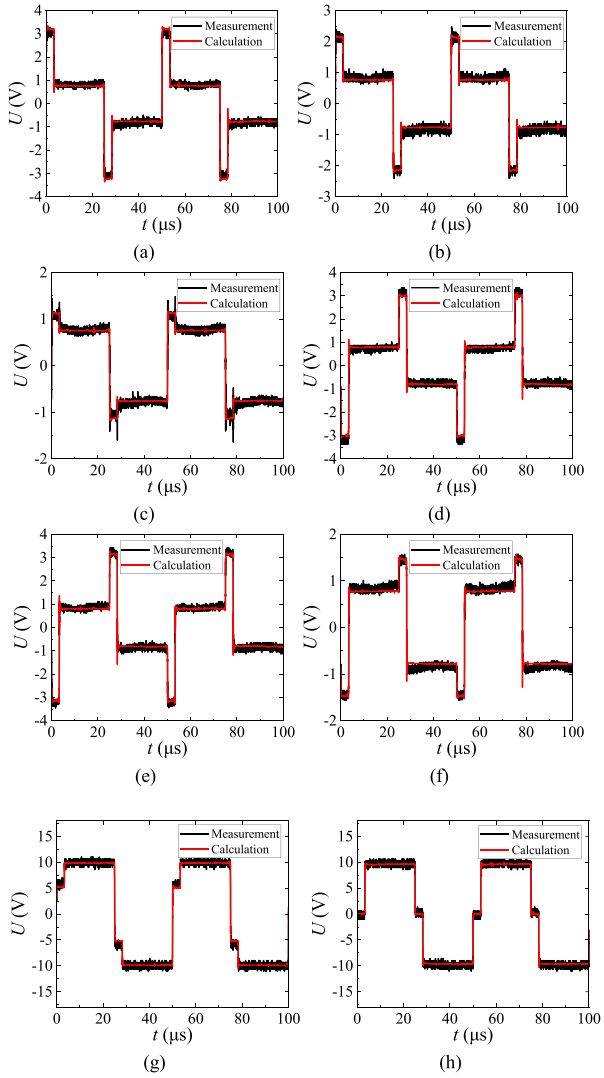

Fig. 13. Measured and calculated EMVs in HFT with separated windings of (a) coil 1, (b) coil 2, (c) coil 4, (d) coil 6, (e) coil 7, (f) coil 8, (g) coil 10, and (h) coil 11 for condition I ($V_\mathrm{pri} = V_\mathrm{sec} = 100$ V, phase shift angle $\varphi = 25°$).

Two error indicators are proposed to evaluate the accuracy of proposed method. The first error indicator is flux density amplitude calculation error (FDACE), which is defined as the error between calculated and measured flux density amplitudes and can be expressed as

$$e_\mathrm{FDACE} = \frac{B_\mathrm{m,cal} - B_\mathrm{m,mea}}{B_\mathrm{m,mea}} \tag{23}$$

where $B_\mathrm{m,cal}$ and $B_\mathrm{m,mea}$ are amplitudes of calculated and measured flux density. B_m can be calculated as

$$B_\mathrm{m} = \frac{\varphi_\mathrm{m}}{S_\mathrm{surface}} = \frac{1}{4 S_\mathrm{surface}} \int_0^T |u_\mathrm{m}(t)| \, \mathrm{d}t \tag{24}$$

where S_surface is the cross-section area, T is the cycle, and $u_\mathrm{m}(t)$ is the equivalent magnetization voltage.

The second error indicator is flux density waveform calculation error (FDWCE), which is defined as the error of areas between calculated and measured flux density waveforms and

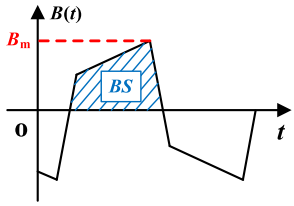

Fig. 14. Schematic diagram of proposed two error indicators.

TABLE II
FLUX DENSITY CALCULATION ERRORS FOR THE HFT WITH SEPARATED WINDINGS FOR CONDITION I ($V_{\mathrm{PRI}} = V_{\mathrm{SEC}} = 100$ V, $\varphi = 25°$)

Coil number	Calculated B_{m} (T)	Measured B_{m} (T)	Errors (%)	Calculated BS (T*μs)	Measured BS (T*μs)	Errors (%)
1	0.2063	0.2127	–3.0	1.178	1.208	–2.4
2	0.1794	0.1927	–6.9	1.019	1.097	–6.9
3	0.1756	0.1837	–4.4	0.9985	1.049	–4.6
4	0.1522	0.1546	–1.5	0.9143	0.9281	–1.6
5	0.1960	0.1912	2.5	1.108	1.088	1.7
6	0.2061	0.2033	1.4	1.169	1.180	–0.86
7	0.2120	0.2214	–4.3	1.203	1.254	–4.1
8	0.1645	0.1746	–5.8	0.9653	1.028	–6.1
9	0.1372	0.1390	–1.3	0.8618	0.8694	–0.96
10	0.1281	0.1299	–1.4	0.8456	0.8520	–0.78
11	0.1160	0.1183	–2.0	0.8217	0.8355	–1.62

can be expressed as

$$e_{\mathrm{FDWCE}} = \frac{BS_{\mathrm{cal}} - BS_{\mathrm{mea}}}{BS_{\mathrm{mea}}} \tag{25}$$

where BS_{cal} and BS_{mea} are areas enclosed by calculated and measured flux density waveforms and t-axis. BS can be calculated as

$$BS = \frac{1}{2}\int_0^T |B(t)|\mathrm{d}t \tag{26}$$

where $B(t)$ is flux density waveform.

The schematic diagram of proposed two error indicators is shown in Fig. 14.

The FDACEs and FDWCEs for the HFT with separated windings ($V_{\mathrm{pri}} = V_{\mathrm{sec}} = 100$ V, phase shift angle $\varphi = 25°$) are listed in Table II. The errors are all below 10% and most of the errors are below 5%.

To further validate the proposed methodology, two other operation conditions are tested. In the first condition (Condition II), the primary and secondary voltage waveforms are square wave. The amplitudes of square voltage are 100 V and the phase shift angle is 10°. In the second condition (Condition III), a 5 μH inductor is connected in series with the primary winding of HFT. The primary voltage waveform of HFT is four-level stair wave and the secondary voltage waveform is square wave. The amplitudes of primary and secondary voltages are 100 V and the phase shift angle is 25°. The waveforms of primary voltage, secondary voltage, secondary current, and coil-1 voltage are shown in Fig. 15. The comparisons of calculated and measured EMVs are shown in Fig. 16. The FDACEs and FDWCEs for the two test conditions are listed in Tables III and IV. The calculation results of EMV waveforms coincide with measurement results. The errors are all below 10% and most of the errors are below 5%. Therefore, the proposed method can accurately calculate the practical flux density distribution.

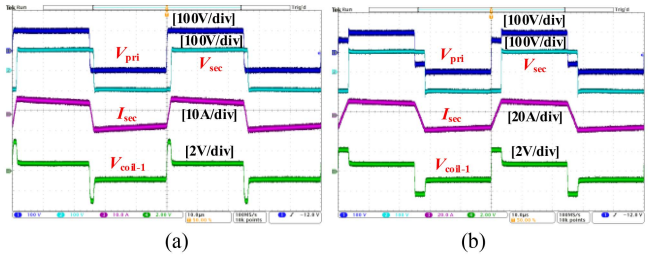

(a) (b)

Fig. 15. Waveforms of primary voltage V_{pri}, secondary voltage V_{sec}, secondary current I_{sec}, and coil-1 voltage $V_{\mathrm{coil\text{-}1}}$ of the HFT with separated windings. (a) Condition II: $V_{\mathrm{pri}} = V_{\mathrm{sec}} = 100$ V, $\varphi = 10°$. (b) Condition III: Series inductance $L_{\mathrm{s}} = 5$ μH, $V_{\mathrm{pri}} = V_{\mathrm{sec}} = 100$ V, $\varphi = 25°$.

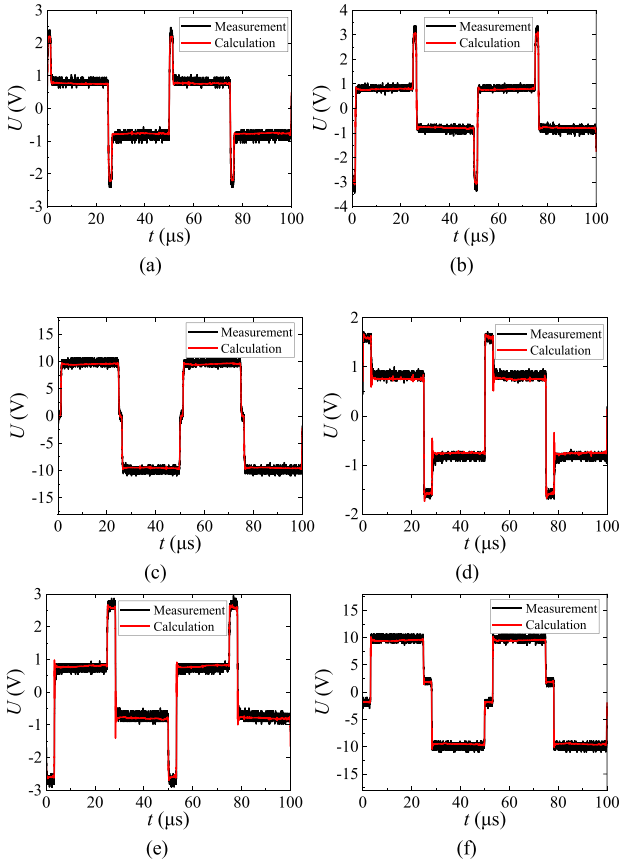

Fig. 16. Measured and calculated EMVs of (a) coil 2, (b) coil 6, (c) coil 11 for condition II ($V_{\mathrm{pri}} = V_{\mathrm{sec}} = 100$ V, $\varphi = 10°$) and (d) coil 2, (e) coil 6, (f) coil 11 for condition III (Series inductance $L_{\mathrm{s}} = 5$ μH, $V_{\mathrm{pri}} = V_{\mathrm{sec}} = 100$ V, $\varphi = 25°$).

TABLE III
FLUX DENSITY CALCULATION ERRORS FOR THE HFT WITH SEPARATED WINDINGS FOR CONDITION II ($V_{\mathrm{PRI}} = V_{\mathrm{SEC}} = 100$ V, $\varphi = 10°$)

Coil number	Calculated B_{m} (T)	Measured B_{m} (T)	Errors (%)	Calculated BS (T*μs)	Measured BS (T*μs)	Errors (%)
1	0.1692	0.1728	-2.1	0.9521	0.9828	-3.1
2	0.1581	0.1707	-7.4	0.9236	0.9952	-7.2
3	0.1561	0.1567	-0.35	0.9145	0.9124	0.24
4	0.1467	0.1452	1.0	0.9006	0.8950	0.62
5	0.1659	0.1779	-6.8	0.9541	1.0394	-8.2
6	0.1710	0.1815	-5.8	0.9738	1.0402	-6.4
7	0.1743	0.1766	-1.3	0.9913	0.9958	-0.45
8	0.1528	0.1616	-5.4	0.9184	0.9759	-5.9
9	0.1353	0.1385	-2.2	0.8491	0.8744	-2.9
10	0.1309	0.1348	-3.0	0.8399	0.8680	-3.2
11	0.1253	0.1298	-3.5	0.8227	0.8547	-3.7

TABLE IV
FLUX DENSITY CALCULATION ERRORS FOR THE HFT WITH SEPARATED WINDINGS FOR CONDITION III ($L_S = 5\ \mu$H, $V_{PRI} = V_{SEC} = 100$ V, $\varphi = 25°$)

Coil number	Calculated B_m (T)	Measured B_m (T)	Errors (%)	Calculated BS (T*μs)	Measured BS (T*μs)	Errors (%)
1	0.1857	0.1891	-1.8	1.0541	1.0720	-1.7
2	0.1639	0.1769	-7.3	0.9504	1.0340	-8.1
3	0.1612	0.1644	-2.0	0.9398	0.9741	-3.5
4	0.1419	0.1411	0.59	0.8846	0.9035	-2.1
5	0.1867	0.1789	4.4	1.0683	1.0268	4.1
6	0.1959	0.1894	3.5	1.1146	1.0889	2.4
7	0.1993	0.2109	-5.5	1.1396	1.1910	-4.3
8	0.1618	0.1656	-2.3	0.9593	0.9668	-0.78
9	0.1279	0.1316	-2.8	0.8364	0.8631	-3.1
10	0.1209	0.1245	-2.9	0.8273	0.8529	-3.0
11	0.1179	0.1223	-3.7	0.8109	0.8442	-3.9

Since surface ribbons saturation effect or nonlinear *B-H* characteristic is not considered in the proposed method, the accuracy of the proposed method may decrease for nanocrystalline core HFT with high leakage inductance or large leakage flux. Future research needs to focus on improved method for flux density distribution calculation considering surface ribbons saturation effect.

D. Comparison With Other Method

The most direct method for calculating flux density distribution in nanocrystalline core of HFT under load condition is time-domain FE simulation method (TD-FEM). The nanocrystalline core is modeled by homogenization method. The HFT is excited by practical excitation voltages. The flux density waveform in nanocrystalline core is calculated by time-domain FE simulation. However, due to the fine meshes and high dV/dt in rising/falling edges of square voltages, time-domain FE simulation requires long computation time, and high computation cost.

Another method for calculating flux density distribution is frequency-domain decomposition-based FE simulation method (FDDE-FEM). The primary voltage $u_p(t)$ is decomposed into high-frequency harmonics $u_{p1}(t)$, $u_{p3}(t)$, … $u_{pn}(t)$ and secondary voltage $u_s(t)$ is decomposed into high-frequency harmonics $u_{s1}(t)$, $u_{s3}(t)$, … $u_{sn}(t)$, where $u_{p1}(t)$, $u_{p3}(t)$, … $u_{pn}(t)$ are the first, third and nth harmonics of primary voltage and $u_{s1}(t)$, $u_{s3}(t)$, … $u_{sn}(t)$ are the first, third and nth harmonics of secondary voltage. Frequency-domain FE simulations are conducted to calculate the flux density distributions under high-frequency harmonic excitations $u_{p1}(t)$ and $u_{s1}(t)$, $u_{p3}(t)$ and $u_{s3}(t)$, … $u_{pn}(t)$ and $u_{sn}(t)$. The practical flux density distribution can be calculated by summation of flux density distributions under all high-frequency harmonic excitations.

These FE models are solved on a server computer (CPU: Intel Xeon E5-2696 v4 at 2.20 GHz; Number of cores: 44; RAM: 1 TB). The model contains 91 451 meshes and 257 412 elements. For TD-FEM, the total solution time is 50 μs and the time step is 0.1 μs. For FDDE-FEM, flux densities under the first 20 harmonic excitations are calculated by parameterized scanning and summarized to obtain the practical flux density. For the proposed method, two frequency-domain FE simulations are conducted, one with open-circuit excitation and the other with short-circuit excitation. The practical flux density is calculated by the method proposed in this article.

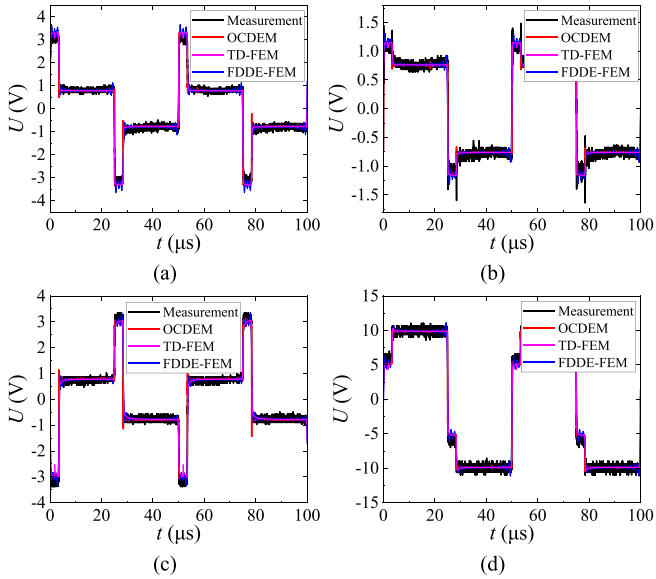

Fig. 17. Measured and calculated EMVs of (a) coil 1, (b) coil 4, (c) coil 6, (d) coil 10 for condition I ($V_{pri} = V_{sec} = 100$ V, $\varphi = 25°$).

TABLE V
COMPARISON OF TD-FEM, FDDE-FEM AND PROPOSED OCDEM

Methods	TD-FEM	FDDE-FEM	OCDEM
|Error of B_m| (%)	<10	<10	<10
|Error of BS|(%)	<10	<10	<10
Computation time	3 h 5 min 9 s	3 h 12 min 48 s	9 min 39 s + 9 min 24 s
Size of model file	20.4 GB	2.48 GB	454 MB
Other	Recalculate when load condition changed		Calculate only once for all load conditions

The comparisons of calculated and measured EMV waveforms are shown in Fig. 17. The calculated EMV waveforms with all the TD-FEM, FDDE-FEM and proposed OCDEM coincide with the measured waveforms. A further comparison of TD-FEM, FDDE-FEM and the proposed OCDEM is shown in Table V. The calculation errors of all these methods are within 8%. However, with TD-FEM, the computation time is 3 h 5 min 9 s and the size of solved model file is 20.4 GB. With FDDE-FEM, the computation time is 3 h 12 min 48 s and the size of solved model file is 2.48 GB. With the proposed OCDEM, the computation time is only 9 min 39 s + 9 min 24 s and the size of solved model file is 454 MB. Both the computation time and size of solved model file with the proposed method are greatly reduced compared with TD-FEM and FDDE-FEM. In addition, with TD-FEM and FDDE-FEM, the model should be recalculated when load condition is changed. However, with the proposed method, only two FE simulations, one with open-circuit excitation and the other with short-circuit excitation, are demanded for flux density calculation under all load conditions. The flux density distribution coefficients are calculated by these two FE simulations and flux density calculation under any load condition can be calculated with the proposed method.

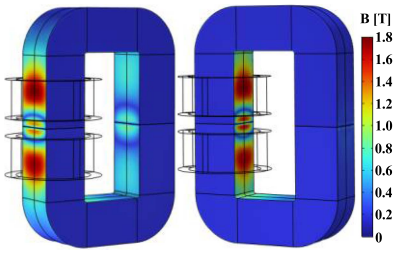

Fig. 18. Flux density amplitude distribution in nanocrystalline core of HFT with separated windings in DAB converter under condition I ($V_{\rm pri} = V_{\rm sec} =$ 100 V, $\varphi = 25°$).

IV. Characterization of Practical Flux Density Distribution

The practical flux density distribution in nanocrystalline core of HFT is nonuniform. In this section, taking DAB converter with SPS modulation as an example, the characteristics of flux density distribution in nanocrystalline core of HFT are investigated.

A. Flux Density Distribution At Different Positions

For DAB converter with SPS modulation, applying (7), the flux density amplitude in different position of the core can be expressed as

$$\begin{aligned} &B_{\rm m}(x,y,z) \\ &= \frac{1}{4}\int_0^T \left|\frac{{\rm d}B(x,y,z,t)}{{\rm d}t}\right| \cdot {\rm d}t \\ &= \frac{1}{4}\int_0^T \left|k_{11}(x,y,z)\frac{{\rm d}\psi_{\rm open}(t)}{{\rm d}t} + k_{22}(x,y,z)\frac{{\rm d}\psi_{\rm short}(t)}{{\rm d}t}\right| \cdot {\rm d}t \\ &= \frac{1}{4}\begin{bmatrix} |k_{11}(x,y,z)U_{\rm open} \pm k_{22}(x,y,z)U_{\rm short}|\, DT \\ +|k_{11}(x,y,z)U_{\rm open}|\,(1-D)T \end{bmatrix} \end{aligned} \tag{27}$$

where D is the phase shift ratio, T is the period, $U_{\rm open}$ is open-circuit voltage amplitude, i.e., amplitude of $u_{\rm AB}$ (t), $U_{\rm short}$ is short-circuit voltage amplitude, i.e., amplitude of $u_{\rm AB}$ (t)-$u_{\rm CD}$ (t), $u_{\rm AB}$ (t), and $u_{\rm CD}$ (t) are waveforms of primary and secondary voltages of HFT, the addition or subtraction "±" depends on the directions of main flux and leakage flux. Applying (27), flux density amplitude distribution in nanocrystalline core is shown in Fig. 18. The flux density is concentrated in surface ribbons of nanocrystalline core near winding ends. The maximum surface flux density amplitude is about 1.8 T, exceeding the saturation flux density of nanocrystalline ribbon, which is typically 1.25 T for Fe-based nanocrystalline alloy composed of $Fe_{73.5}Cu_1Nb_3Si_{15.5}B_7$. The surface ribbon saturation is not considered in this methodology due to its nonlinear characteristic and complex computation. Taking position 1 shown in Fig. 7(b), as an example, the EMV waveforms of the nth 0.02 mm-thickness ribbons in inner surface of the core are shown in Fig. 19(a). The voltage amplitudes of surface ribbons in the phase-offset stage (stage 2) is higher than interior ribbons. In addition, the voltage amplitude in the phase-offset stage (stage 2) is higher for the ribbon closer to the surface.

As shown in Fig. 19(b), average flux density amplitude decreases with the number of surface ribbon layer. The highest flux density amplitude is 0.86 T in the first layer of surface ribbon. In addition, average flux density amplitude in the surface 1 mm-thickness ribbons (about 50 layers) is 0.29 T. However, average flux density amplitude in the interior ribbon is about 0.12 T. The surface flux density will be significantly underestimated without considering the nonuniform distribution characteristics of practical flux density.

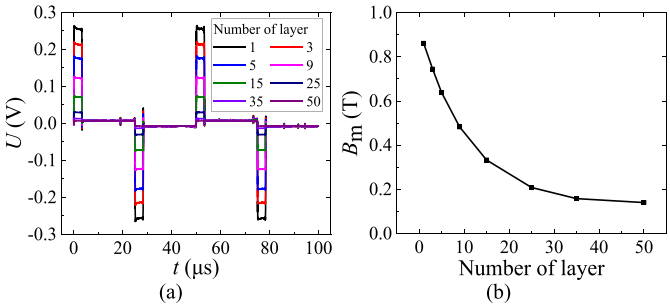

Fig. 19. (a) EMV waveforms of the nth 0.02 mm thick ribbons in the inner surface of the core and (b) variation of average flux density amplitude with the number of surface layer.

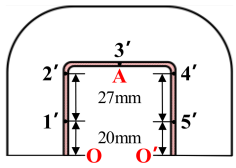

Fig. 20. Dimensions of 5 positions and path OAO' in upper part of the core.

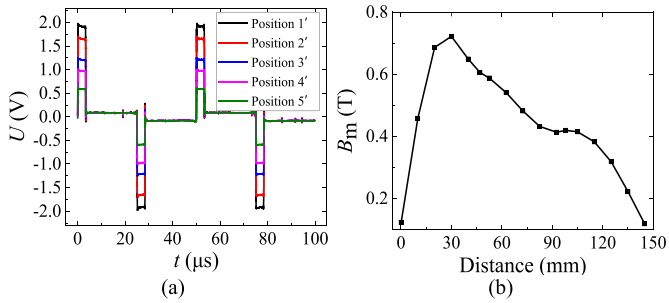

Fig. 21. (a) EMV waveforms at 5 different positions in the inner surface of the core. (b) Variation of average flux density amplitude along the path OAO'.

Taking 0.2 mm-thickness cross-sections in inner surface of the core, as an example, Fig. 21(a) shows the EMV waveforms at 5 different positions, as shown in Fig. 20. Since the physical structure of the HFT prototype is symmetrical, only upper part of the core is analyzed. EMV amplitude of P1' is the highest and EMV amplitude of P5' is the lowest in the phase-offset stage (stage 2). Fig. 21(b) shows the variation of average flux density amplitude along path OAO'. Average flux density amplitude first increases and then decreases along OAO'. In addition, average flux density amplitude near winding end is the highest. Since average flux density amplitude in the interior ribbon is 0.12 T, surface flux density will be significantly underestimated without considering the nonuniform distribution characteristics of practical flux density.

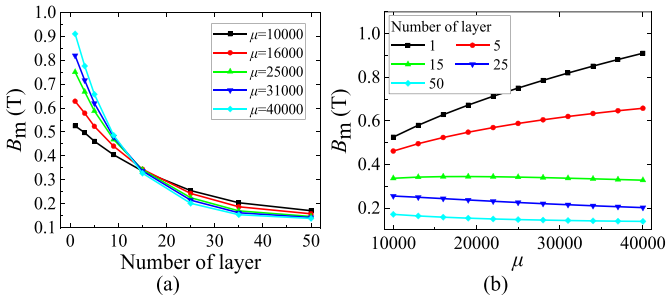

Fig. 22. Variation of average flux density amplitude with. (a) Number of surface ribbon layer. (b) Permeability.

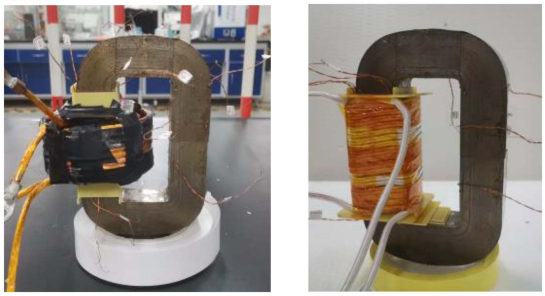

Fig. 23. Photograph of (a) HFT prototype with concentric windings and (b) HFT prototype with interleaved windings.

B. Impact of Permeability on Flux Density Distribution

Temperature and frequency can significantly change the permeability of nanocrystalline ribbon, thereby change the practical flux density distribution in the core. Taking position 1 shown in Fig. 7(b), as an example, Fig. 22(a) and (b) shows the variation of average flux density amplitude with the number of surface ribbon layer and permeability. As shown in Fig. 22(a), average flux density amplitude decreases with the number of surface ribbon layer. As shown in Fig. 22(b), average flux density amplitude in the first and fifth surface ribbon layers increases with permeability and average flux density amplitude in the 15th, 25th, and 50th surface ribbon layers decreases with permeability. When permeability increases from 10 000 to 40 000, average flux density amplitude in the first surface ribbon layer is increased by 0.73 times. The reason is that the leakage flux penetrating internal ribbons decreases with permeability. Surface leakage flux density increases with permeability and interior leakage flux density decreases with permeability.

C. Comparison of Flux Density Distribution Between Different Winding Structures

Since leakage flux density distribution in surface ribbons of nanocrystalline core is sensitive to winding and core structures, practical flux density distribution in nanocrystalline core is also dependent on transformer structures. Two other HFTs with different winding structures are prototyped, as shown in Fig. 23(a) and (b). The first HFT prototype shown in Fig. 23(a) is made with concentric windings. The turns of both primary and secondary windings are 9. The leakage inductance is 5.9 μH measured by an impedance analyzer. The second HFT prototype shown in Fig. 23(b) is made with interleaved windings. The turns of both primary and secondary windings are also 9. The leakage inductance is 0.9 μH measured by an impedance analyzer.

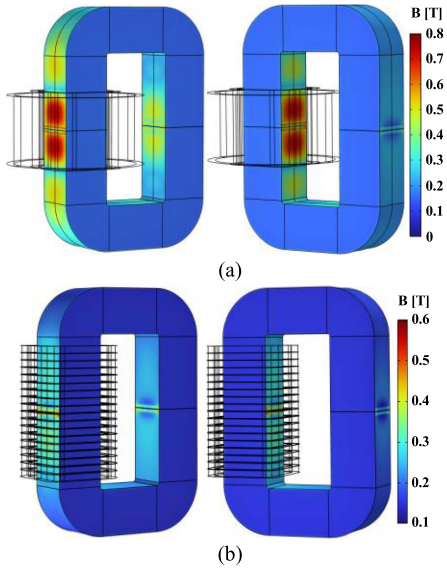

Fig. 24. Flux density amplitude distribution in (a) nanocrystalline core of HFT with concentric windings in DAB converter ($V_{\rm pri} = V_{\rm sec} = 100$ V, $\varphi = 10°$) and (b) nanocrystalline core of HFT with interleaved windings in DAB converter ($V_{\rm pri} = V_{\rm sec} = 100$ V, $L_{\rm s} = 10$ μH, $\varphi = 10°$).

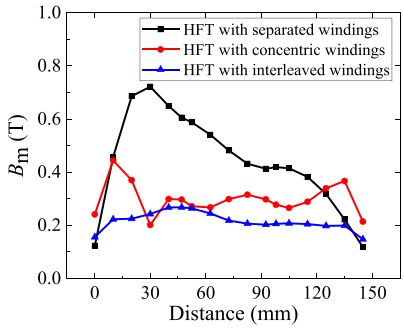

Fig. 25. Comparison of average flux density amplitudes along path OAO' for the three HFT prototypes.

Applying the proposed flux density distribution calculation method and (27), flux density amplitude distributions in nanocrystalline core of HFT with concentric windings and interleaved windings are shown in Fig. 24(a) and (b), respectively. For both HFT prototypes, the flux densities are concentrated in surface ribbons of the core surrounded by the windings. The flux density amplitudes in interior ribbons are about 0.14 T. For the HFT with concentric windings, the maximum flux density amplitude in surface ribbons is about 0.75 T. For the HFT with interleaved windings, the maximum flux density amplitude in surface ribbons is about 0.3 T. Taking the 0.2 mm-thickness cross-sections in the inner surface of the core, as shown in Fig. 20, as an example, the comparison of average flux density amplitudes along path OAO' for the three HFT prototypes is shown in Fig. 25. The average flux density amplitude in surface ribbons for the HFT with separated windings is the highest,

TABLE VI
THERMAL TEST CONDITIONS FOR THE HFTS WITH SEPARATED WINDINGS

	Open-circuit condition	Load condition
Nanocrystalline core HFT	$U = 150$V	$U = 150$V, $\varphi = 25°$
Ferrite core HFT	$U = 150$V	$U = 150$V, $\varphi = 25°$

while that for the HFT with interleaved windings is the lowest. The reason is that the HFT with separated windings has the highest leakage flux or leakage inductance, while the HFT with interleaved windings has the lowest leakage flux or leakage inductance. Since the leakage flux density in surface ribbons of the core is determined by the leakage flux of HFT, the HFT with separated windings has the highest surface leakage flux density, while the HFT with interleaved windings has the lowest surface leakage flux density.

V. DISCUSSION

The practical nonuniform flux density distribution in nanocrystalline core can have significant impact on core loss. First, since leakage flux is mainly concentrated in the surface of the core, by magnetic flux superposition principle, the practical flux density amplitude in surface ribbons is higher than interior ribbons. Thus, the magnetic loss in surface ribbons is higher than internal ribbons. Second, normal leakage flux in the surface of the core can induce eddy currents in surface ribbons, bringing significant leakage flux eddy current loss. Therefore, the power loss of surface ribbons can be significantly higher than interior ribbons, increasing the total power loss of nanocrystalline core under load condition. Traditional core loss calculation methods for open-circuit excitations will underestimate the core loss. To illustrate the differences in core losses between open-circuit condition and practical load condition, temperature tests by infrared camera and calorimetric measurements of nanocrystalline core losses are conducted in this section. The infrared thermal tests can provide overall temperature distributions in the core, which is correlated to core loss density distributions, and the calorimetric measurements can provide precise values and comparisons of core losses under open-circuit and load conditions.

A. HFT Temperature Tests By Infrared Camera

Two thermal test conditions for the HFT prototypes with separated windings are selected in this article, including open-circuit conditions and load conditions, as listed in Table VI. The selected load condition is a DAB converter with SPS modulation. The cooling conditions are natural cooling. For comparison, a ferrite core HFT with the same core and winding structures is also made and tested. The surfaces of the HFTs are coated with a high-emissivity coating with an emissivity of 0.94. An infrared camera is used to measure the steady-state temperature distributions of HFTs.

As shown in Fig. 26(a) and (b), for the nanocrystalline core HFT, temperature difference between inner and outer sides of the core is -3 °C to -2 °C under open-circuit condition and 5 °C to 10 °C under load condition. In addition, core temperature

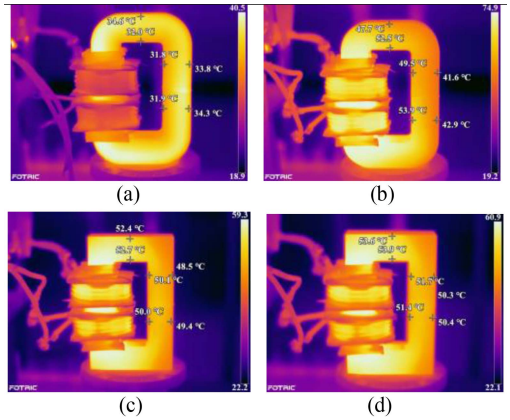

Fig. 26. Temperature distributions of (a) nanocrystalline core HFT under open-circuit condition, (b) nanocrystalline core HFT under load condition, (c) ferrite core HFT under open-circuit condition, and (d) ferrite core HFT under load condition.

under load condition is more than 10 °C higher than open-circuit condition. As shown in Fig. 26(c) and (d), for the ferrite core HFT, temperature differences between inner and outer sides of the core are below 2 °C under open-circuit and load conditions.

There are two aspects to prove that the observed temperature differences between open-circuit and load conditions for nanocrystalline core HFT are a consequence of additional core loss caused by nonuniform leakage flux density distribution instead of winding loss. First, the winding loss is small compared with core loss. As measured by calorimetric method to be discussed in Section V-B, for the nanocrystalline core HFT, the open-circuit core loss, loaded core loss and winding loss are estimated to be 4.77 W, 13.66 W, and 3.09 W, respectively. The core loss caused by nonuniform flux density distribution is about 8.89 W. The winding losses are small and the thermal resistances between core and windings are large. Therefore, the impact of winding loss on core temperature is small. Second, as shown in Fig. 26(c) and (d), for ferrite core HFT, the temperature differences of the ferrite cores between inner and outer sides and between open-circuit and load conditions are small. The comparison of temperature distributions between nanocrystalline core and ferrite core HFTs indicates that the winding loss under load condition will not result in significant temperature nonuniformity between inner and outer sides of the core and significant temperature rise under load condition. Therefore, the nonuniform temperature distribution and temperature rise in nanocrystalline core should be attributed to the additional core loss under load condition.

B. Calorimetric Measurement of Core Loss

Since HFT power loss under load condition cannot be accurately measured by electrical method, calorimetric method is adopted for HFT power loss measurement. For loaded core loss measurement, the primary and secondary windings of HFT are excited by square voltages with a phase shift angle. The HFT total power loss P_t is measured with calorimetric method and winding loss P_w is calculated by summation of winding losses under all harmonic current excitations with superposition

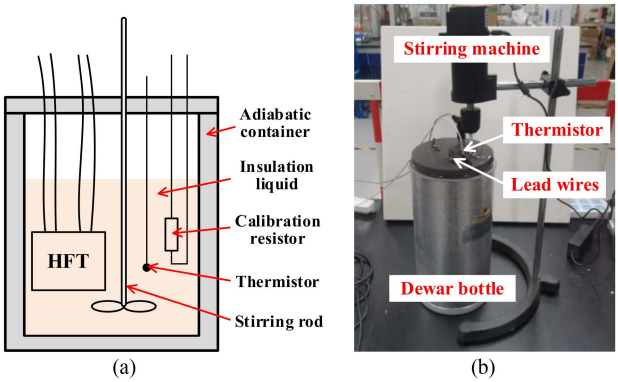

Fig. 27. (a) Schematic diagram. (b) Experimental setup of calorimeter.

TABLE VII
CORE LOSS MEASUREMENT RESULTS FOR THE HFT WITH SEPARATED WINDINGS

Load conditions	B_{main} (T)	P_{load} (W)	P_{main} (W)	P_{leak} (W)	P_{leak}/P_{load} (%)
U_m=300 V, φ=15°	0.52	87.63	41.46	46.17	52.69
U_m=250 V, φ=20°	0.43	74.09	29.15	44.94	60.66
U_m=250 V, φ=15°	0.43	58.21	29.15	29.06	49.92
U_m=200 V, φ=25°	0.35	54.62	19.06	35.56	65.10
U_m=200 V, φ=15°	0.35	35.01	19.06	15.95	45.56
U_m=150 V, φ=20°	0.26	22.73	10.81	11.92	52.44

method. Core loss P_c can be calculated by (28). For open-circuit core loss measurement, the secondary winding of HFT is open-circuited and primary winding is excited by square voltage. The total HFT power loss P_t and primary winding loss P_w can also be measured with calorimetric method and calculated by superposition method. Core loss P_c can also be calculated by

$$P_c = P_t - P_w. \tag{28}$$

A calorimeter, as shown in Fig. 27, is designed for HFT power loss measurement. The working principle of the calorimeter, measurement procedures of HFT total power loss P_t with calorimetric method, and calculation method of winding loss P_w are described in detail in our previous paper [24].

After calculating the loaded core loss by (28), the leakage flux induced power loss P_{leak} can be calculated by

$$P_{leak} = P_{load} - P_{main} \tag{29}$$

where P_{load} is core loss under load condition and P_{main} is main flux induced core loss under open-circuit condition.

The measured P_{load}, P_{main}, and P_{leak} for the two HFT prototypes at different square voltage amplitudes U_m or main flux density amplitudes B_m, phase shift angles φ, and primary side series inductance L_s are listed in Tables VII and VIII. The operating frequencies of HFTs in the experimental tests are 20 kHz. For the HFT with separated windings, the proportions of P_{leak} in P_{load} can reach 50%–65%, while for the HFT with concentric windings, the proportions of P_{leak} in P_{load} can reach 10%–25%. The leakage flux induced power loss is a significant component in the total core loss of nanocrystalline core HFT under load condition. In addition, leakage flux induced power loss for the HFT with separated windings is higher than the HFT with concentric windings. The reason is that the HFT with separated windings has higher leakage flux than the HFT with concentric windings.

TABLE VIII
CORE LOSS MEASUREMENT RESULTS FOR THE HFT WITH CONCENTRIC WINDINGS

Load conditions	B_{main} (T)	P_{load} (W)	P_{main} (W)	P_{leak} (W)	P_{leak}/P_{load} (%)
U_m=300 V, φ=5°, L_s=0 μH	0.58	68.70	55.00	13.70	19.94
U_m=300 V, φ=10°, L_s=5 μH	0.58	67.34	55.00	12.34	18.32
U_m=300 V, φ=15°, L_s=15 μH	0.58	63.18	55.00	8.18	12.95
U_m=250 V, φ=5°, L_s=0 μH	0.48	46.40	37.75	8.65	18.64
U_m=250 V, φ=25°, L_s=15 μH	0.48	48.88	37.75	11.13	22.77
U_m=200 V, φ=15°, L_s=5 μH	0.39	32.68	23.82	8.86	27.11

VI. CONCLUSION

This article proposes an accurate and efficient calculation method of practical flux density distribution in nanocrystalline core of HFT under load condition and further investigates the flux density distribution characteristics. The main conclusions are listed as follows.

1) An efficient flux density distribution calculation method for nanocrystalline core of HFT under load condition is proposed. The flux density calculation errors with the proposed OCDEM are all within 10%, and most of the errors are within 5%. Compared with TD-FEM and FDDE-FEM, the proposed OCDEM greatly reduces the computation time and achieves high calculation accuracy.
2) In DAB converter with SPS modulation, flux variation rate $d\phi(t)/dt$ of surface ribbons in nanocrystalline core are four-level stair wave instead of square wave. The practical flux density distribution in nanocrystalline core of HFT under load condition is nonuniform and different from open-circuit condition.
3) The practical flux density distribution in nanocrystalline core varies with positions, permeability, and transformer structure. Flux density amplitudes in surface ribbons are higher than interior ribbons and flux density amplitude in surface ribbons around winding end is higher than other positions. In addition, flux density amplitude in surface ribbons increases with permeability and that in interior ribbons decreases with permeability. Furthermore, flux density amplitudes for the HFT with separated windings are higher than the HFT with concentric windings.
4) Compared with open-circuit condition, the nonuniform flux density distribution in nanocrystalline core of HFT under load condition increases core loss and temperature. The nonuniform flux density distribution should be taken into considerations for accurate core loss estimation.

The practical nonuniform flux density distribution can increase nanocrystalline core loss [24]. An accurate understanding of the nonuniform flux density distribution is the foundation of accurate core loss estimation. The proposed OCDEM and flux density distribution characteristics can guide the power loss optimization and thermal design of nanocrystalline core HFT.

REFERENCES

[1] B. Zhao, Q. Song, W. Liu, and Y. Sun, "Overview of dual-active bridge isolated bidirectional DC–DC converter for high-frequency-link power-conversion system," *IEEE Trans. Power Electron.*, vol. 29, no. 8, pp. 4091–4106, Aug. 2014.

[2] Y. Shi, R. Li, Y. Xue, and H. Li, "Optimized operation of current-fed dual active bridge DC-DC converter for PV applications," *IEEE Trans. Ind. Electron.*, vol. 62, no. 11, pp. 6986–6995, Nov. 2015.

[3] X. Wang, J. Liu, S. Ouyang, T. Xu, F. Meng, and S. Song, "Control and experiment of an H-bridge-based three-phase three-stage modular power electronic transformer," *IEEE Trans. Power Electron.*, vol. 31, no. 3, pp. 2002–2011, Mar. 2016.

[4] C. Gu, Z. Zheng, L. Xu, K. Wang, and Y. Li, "Modeling and control of a multiport Power Electronic Transformer (PET) for electric traction applications," *IEEE Trans. Power Electron.*, vol. 31, no. 2, pp. 915–927, Feb. 2016.

[5] T. Liu et al., "Design and implementation of high efficiency control scheme of dual active bridge based 10 kV/1 MW solid state transformer for PV application," *IEEE Trans. Power Electron.*, vol. 34, no. 5, pp. 4223–4238, May 2019.

[6] Y. Cao, K. Ngo, and D. Dong, "A scalable electronic-embedded transformer, a new concept toward ultra-high-frequency high-power transformer in DC–DC Converters," *IEEE Trans. Power Electron.*, vol. 38, no. 8, pp. 9278–9293, Aug. 2023.

[7] B. Zhao, Q. Song, J. Li, W. Liu, G. Liu, and Y. Zhao, "High-frequency link DC transformer based on switched capacitor for medium-voltage DC power distribution application," *IEEE Trans. Power Electron.*, vol. 31, no. 7, pp. 4766–4777, Jul. 2016.

[8] A. Jafari, M. S. Nikoo, F. Karakaya, and E. Matioli, "Enhanced dab for efficiency preservation using adjustable-tap high-frequency transformer," *IEEE Trans. Power Electron.*, vol. 35, no. 7, pp. 6673–6677, Jul. 2020.

[9] Z. Guo, R. Yu, W. Xu, X. Feng, and A. Q. Huang, "Design and optimization of a 200-kW medium-frequency transformer for medium voltage SiC PV inverters," *IEEE Trans. Power Electron.*, vol. 36, no. 9, pp. 10548–10560, Sep. 2021.

[10] B. S. Ram, A. K. Paul, and S. V. Kulkarni, "Soft magnetic materials and their applications in transformers," *J. Magnetism Magn. Mater.*, vol. 537, Nov. 2021, Art. no. 168210.

[11] A. Garcia-Bediaga, I. Villar, A. Rujas, L. Mir, and A. Rufer, "Multiobjective optimization of medium-frequency transformers for isolated soft-switching converters using a genetic algorithm," *IEEE Trans. Power Electron.*, vol. 32, no. 4, pp. 2995–3006, Apr. 2017.

[12] B. Chen, X. Liang, and N. Wan, "Design methodology for inductor-integrated litz-wired high-power medium-frequency transformer with the nanocrystalline core material for isolated DC-link stage of solid-state transformer," *IEEE Trans. Power Electron.*, vol. 35, no. 11, pp. 11557–11573, Nov. 2020.

[13] Z. Li, E. Hsieh, Q. Li, and F. C. Lee, "High-frequency transformer design with medium-voltage insulation for resonant converter in solid-state transformer," *IEEE Trans. Power Electron.*, vol. 38, no. 8, pp. 9917–9932, Aug. 2023.

[14] N. Rasekh, J. Wang, and X. Yuan, "The variation of core loss in high frequency transformers under different load conditions," in *Proc. 24th Eur. Conf. Power Electron. Appl.*, 2022, pp. P.1–P.10.

[15] N. Rasekh, J. Wang, and X. Yuan, "Variation of core loss in high frequency transformers under different load conditions," *IEEE Open J. Ind. Electron. Soc.*, vol. 4, pp. 316–327, 2023.

[16] J. Wang, H. Lin, Y. Huang, and X. Sun, "A new formulation of anisotropic equivalent conductivity in laminations," *IEEE Trans. Magn.*, vol. 47, no. 5, pp. 1378–1381, May 2011.

[17] Y. Wang, G. Calderon-Lopez, and A. J. Forsyth, "High-Frequency Gap Losses in Nanocrystalline Cores," *IEEE Trans. Power Electron.*, vol. 32, no. 6, pp. 4683–4690, Jun. 2017.

[18] G. Calderon-Lopez, Y. Wang, and A. J. Forsyth, "Mitigation of Gap Losses in Nanocrystalline Tape-Wound Cores," *IEEE Trans. Power Electron.*, vol. 34, no. 5, pp. 4656–4664, May 2019.

[19] H. Sun, Y. Li, Z. Lin, Z. Wan, and H. Liu, "Loss modeling and reluctance quantifying of C-type amorphous core for high-frequency inductors," *IEEE J. Emerg. Sel. Topics Power Electron.*, vol. 11, no. 1, pp. 691–700, Feb. 2023.

[20] R. B. Beddingfield, A. M. Leary, R. Noebe, M. Nations, R. Bowman, and S. Bhattacharya, "Calculation of transformer leakage inductance by simplified flux path geometries," in *Proc. IEEE Energy Convers. Congr. Expo.*, Oct. 2022, pp. 1–8.

[21] C. Chen, Z. Guo, R. Yu, and A. Q. Huang, "A novel hybrid core structure for 100kW medium frequency transformers," in *Proc. IEEE Energy Convers. Congr. Expo.*, Oct. 2023, pp. 5651–5657.

[22] X. Liu, L. Zhao, C. Ma, Q. Ge, and Y. Li, "Optimization simulation analysis of leakage magnetic field and loss characteristics of high frequency nanocrystalline transformer," in *Proc. 25th Int. Conf. Elect. Machines Syst.*, Nov. 2022, pp. 1–6.

[23] Z. Liu, L. Zhu, Y. Dang, C. Zhan, and S. Ji, "Deduction measurement method and high-accuracy calculation model of leakage flux eddy current loss in nanocrystalline core high-frequency transformer," *IEEE Trans. Power Electron.*, vol. 40, no. 4, pp. 5609–5621, Apr. 2025.

[24] Z. Liu, L. Zhu, Y. Dang, and S. Ji, "Core Loss calculation method considering leakage flux induced power loss for nanocrystalline core high-frequency transformer under load condition," *IEEE Trans. Power Electron.*, vol. 40, no. 9, pp. 13126–13141, Sep. 2025.

Zhanlei Liu (Graduate Student Member, IEEE) was born in Hebei, China, in 1998. He received the B.S. degree in electrical engineering in 2020 from Xi'an Jiaotong University, Xi'an, China, where he is currently working toward the Ph.D. degree in electrical engineering.

His research interests include modeling of high-frequency magnetic materials and thermal design of high-frequency transformers.

Lingyu Zhu (Senior Member, IEEE) was born in Shandong, China, in 1988. He received the B.Sc. and Ph.D. degrees in electrical engineering from Xi'an Jiaotong University, Xi'an, China, in 2009 and 2014, respectively.

He is currently a Full Professor with Xi'an Jiaotong University, Xi'an, China. His research interests include condition monitoring of power equipment in HVDC application.

Yongliang Dang was born in Gansu, China, in 1996. He received the B.S. degree in electrical engineering in 2018 from Xi'an Jiaotong University, Xi'an, China, where he is currently working toward the Ph.D. degree in electrical engineering.

His research interests include modeling of high frequency magnetic component in power electronic equipment.

Shengchang Ji (Member, IEEE) was born in Shandong, China, in 1976. He received the B.Sc. and Ph.D. degrees in electrical engineering from Xi'an Jiaotong University, China, in 1998 and 2003, respectively.

He is currently a Professor with Xi'an Jiaotong University, Xi'an, China. His research interests include condition monitoring of power equipment in HVDC application.